Structural Steering of Bismuth Chalcogenides to Oriented Bismuth Catalyst toward Efficient CO_2 Reduction

Yao Xia[a,c], *Jiacheng Liu*[a,c], *Guodong Wu*[a], *Ying Shi*[a], *Dingding Dong*[a], *Junpeng Liu*[a], *Chi Wang*[b], *Dandan Feng*[b], *Yu Su**[b], *Huiwen Lin**[a]

[a] School of Materials Science and Engineering, Southeast University, Nanjing 211189, PR China

[b] School of Science, China Pharmaceutical University, Nanjing 211198, PR China

[c] These authors contribute equally.

Corresponding E-mail addresses: suyu@cpu.edu.cn; linh@seu.edu.cn

KEYWORDS: Electrochemical carbon dioxide reduction; electrochemical reconstruction; bismuth chalcogenide, structural steering

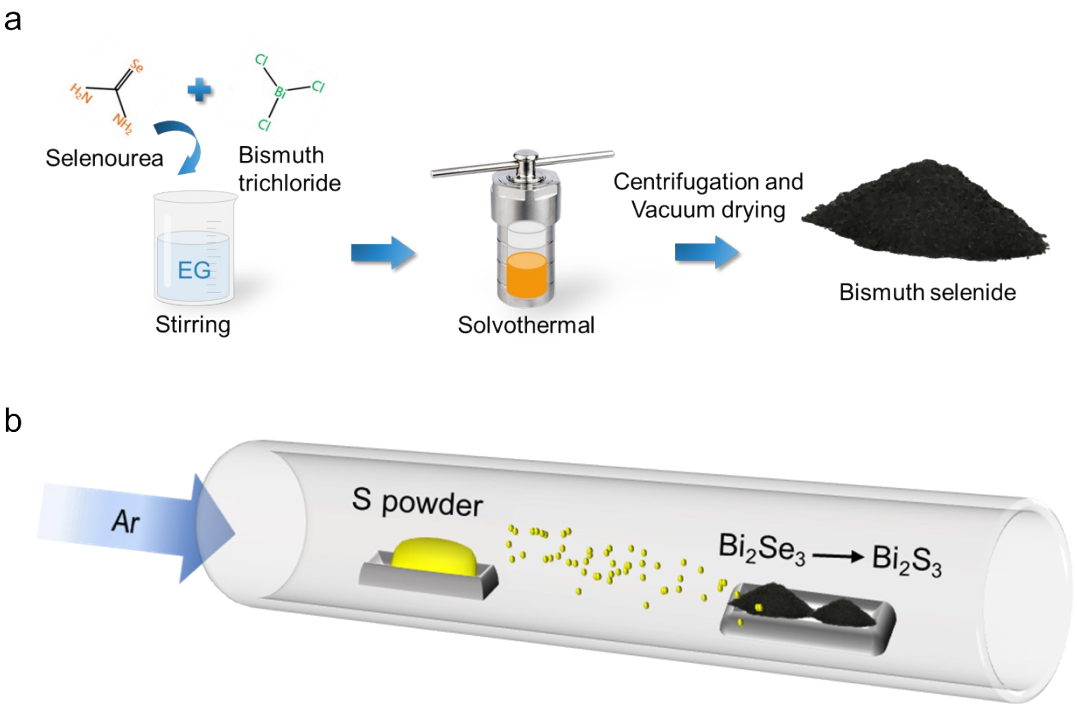

Figure S1. Schematic illustration of the hydrothermal process for the preparation of (a) Bi_2Se_3, and (b) Bi_2S_3 nanosheets.

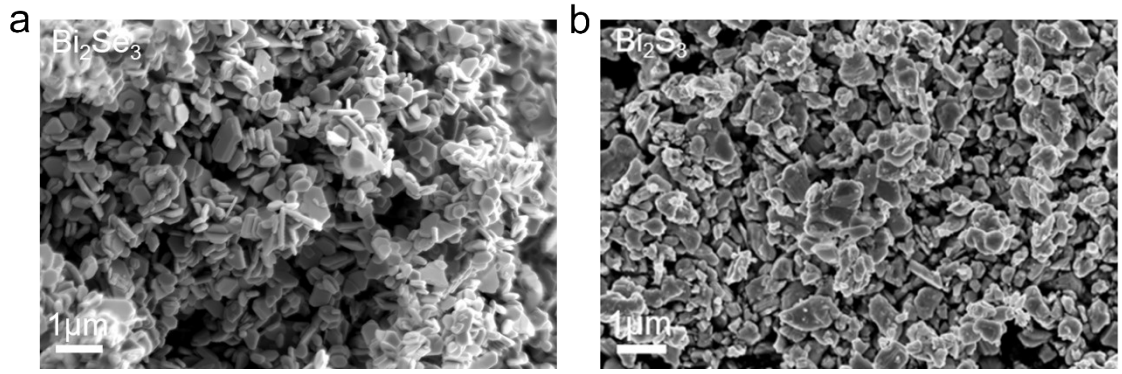

Figure S2. SEM images of nanosheets. (a) Bi_2Se_3, and (b) Bi_2S_3.

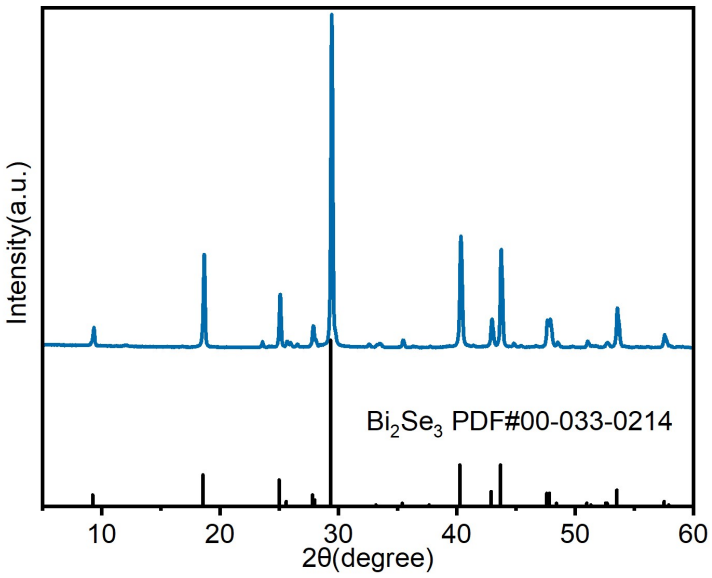

Figure S3. XRD pattern of Bi_2Se_3.

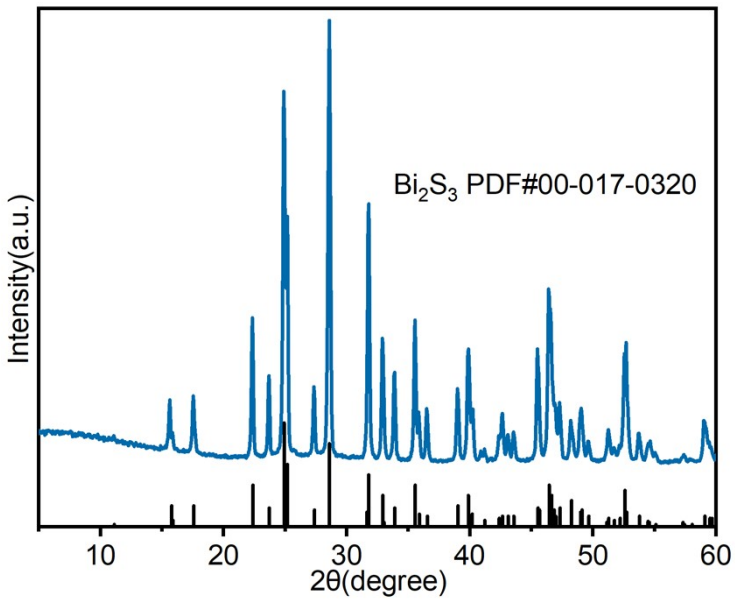

Figure S4. XRD pattern of Bi_2S_3.

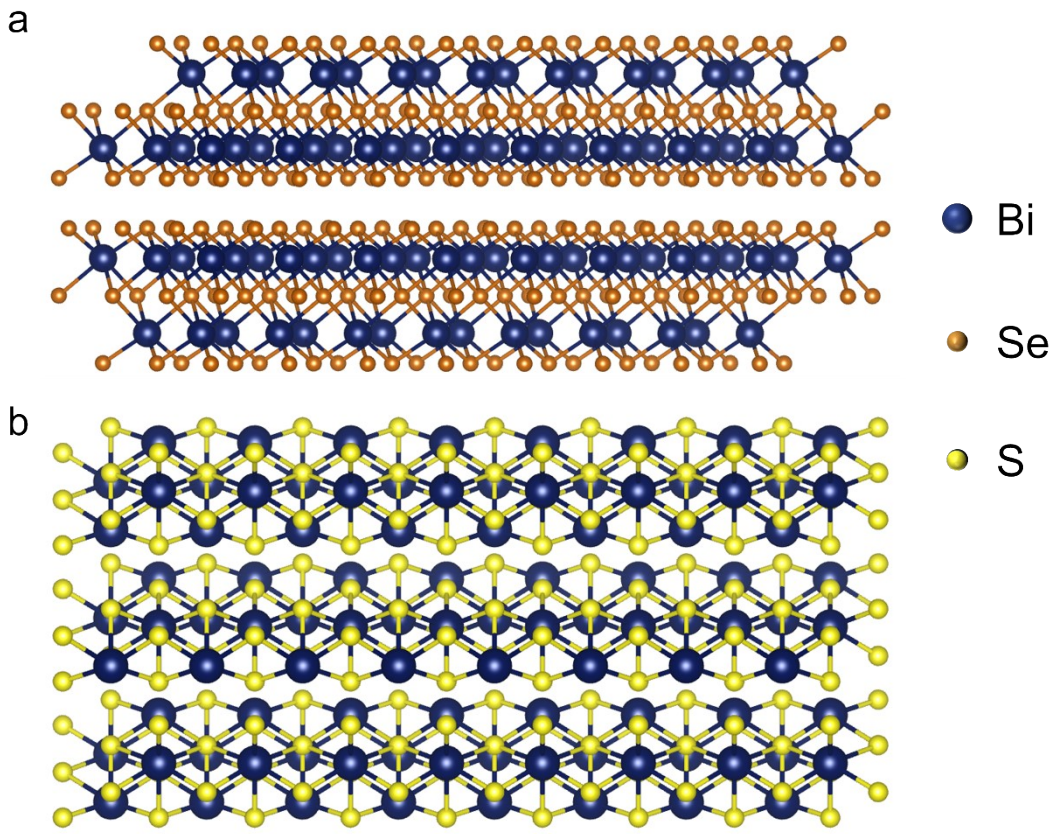

Figure S5. Schematic illustration of the atomic structure of (a) Bi_2Se_3, (b) Bi_2S_3.

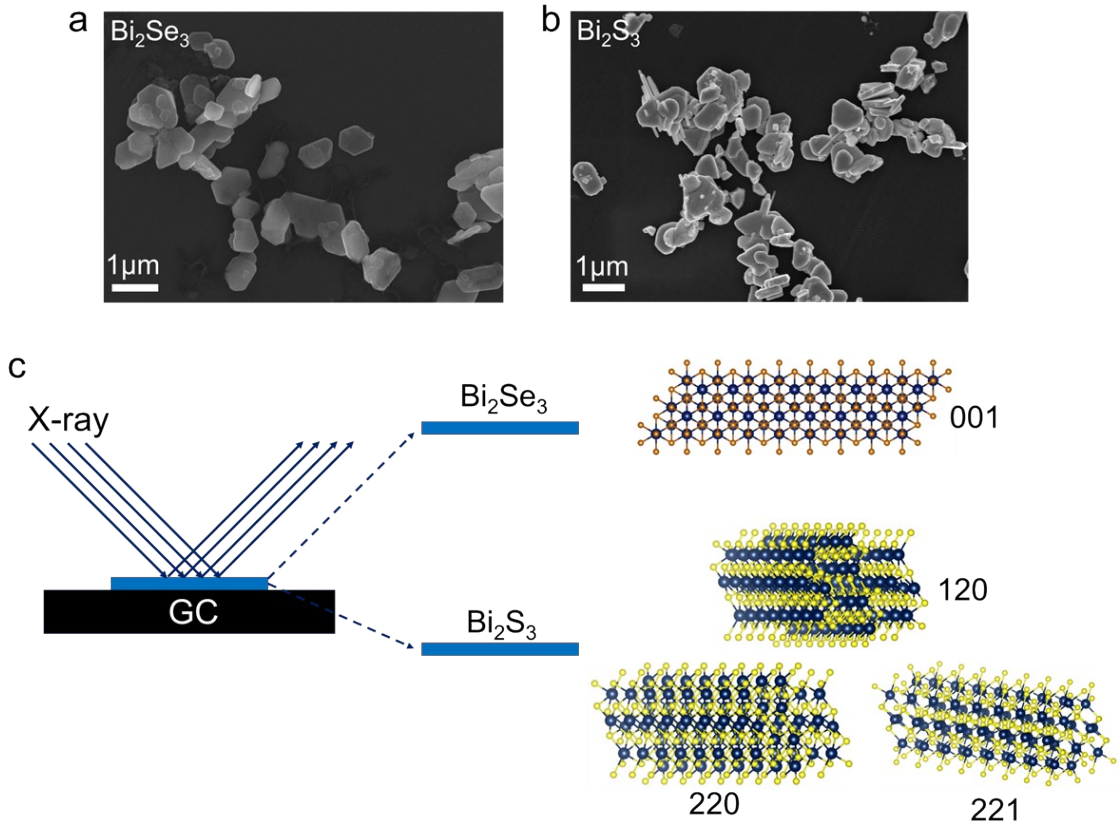

Figure S6. SEM images of (a) Bi_2Se_3, (b) Bi_2S_3 inks spin-coated onto a smooth glassy carbon electrode. (c) Schematic illustration of XRD diffraction and the exposed specific crystal planes of the catalyst.

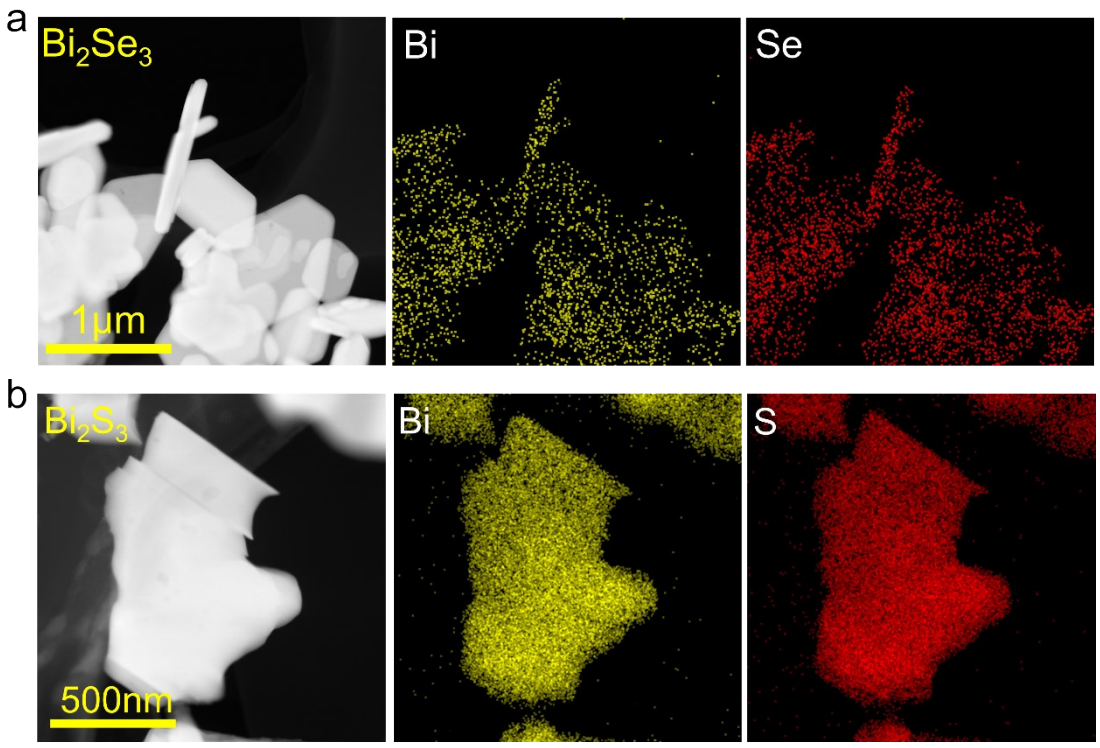

Figure S7. TEM images of (a) Bi_2Se_3, (b) Bi_2S_3 nanosheets, and EDS elemental maps.

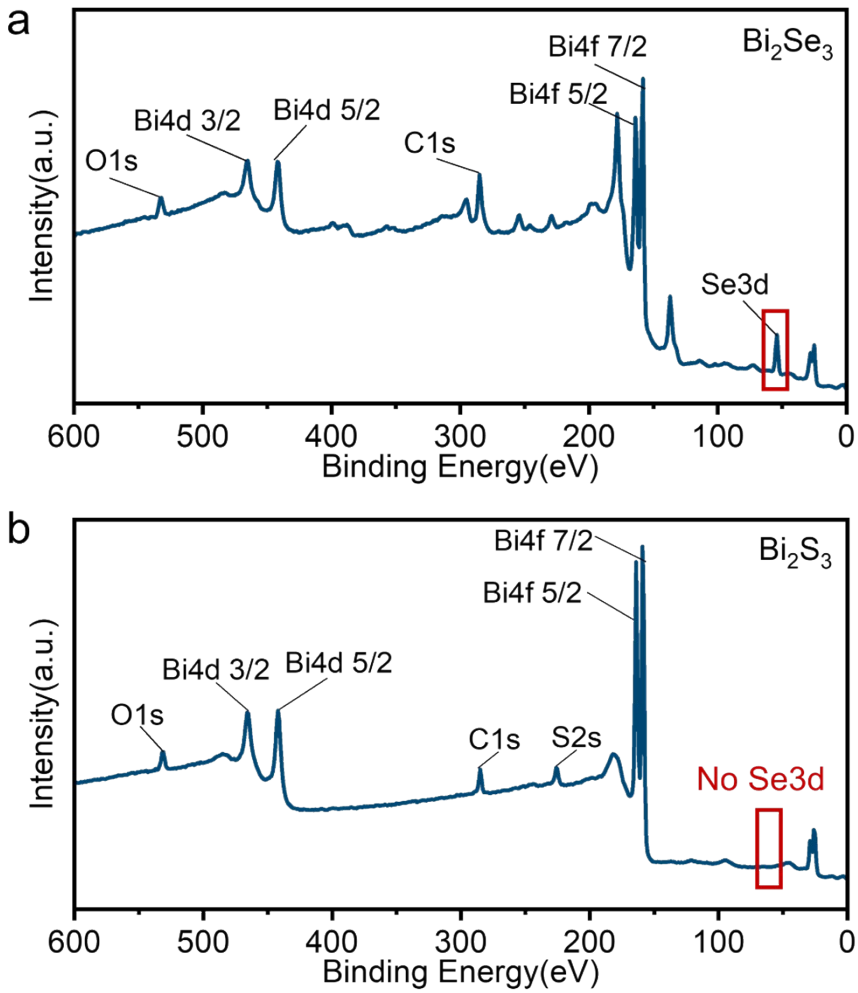

Figure S8. Full spectra of the high-resolution XPS profiles for (a) Bi_2Se_3, (b) Bi_2S_3.

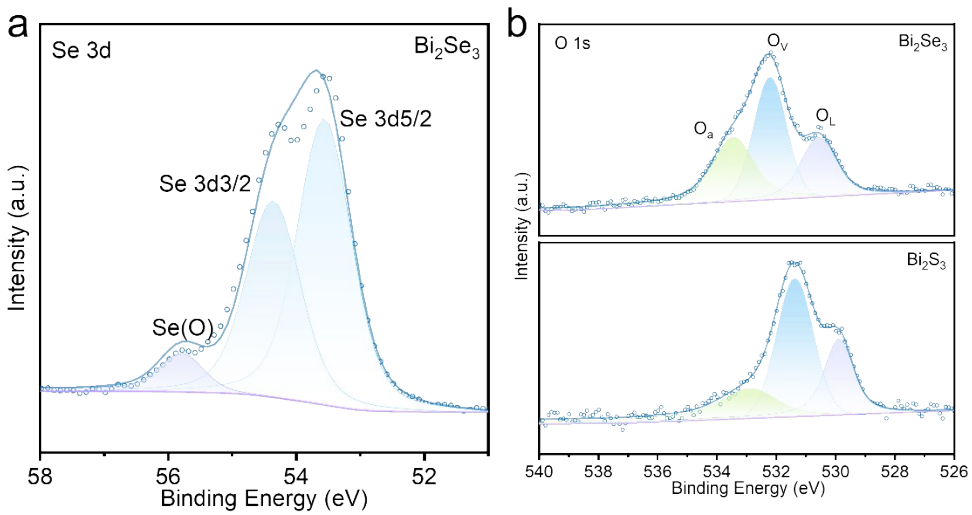

Figure S9. (a) High-resolution XPS spectra of Se 3d. (b) High-resolution XPS spectra of O 1s for Bi_2Se_3 and Bi_2S_3.

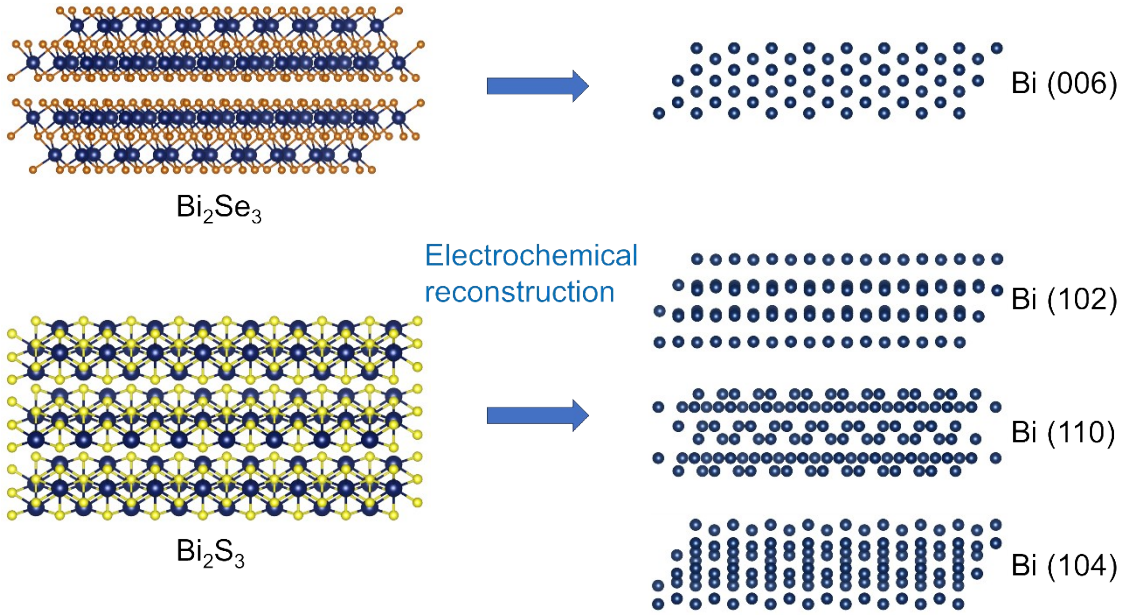

Figure S10. Schematic illustration of the electrochemical reconstruction process of Bi_2Se_3 and Bi_2S_3 on a glassy carbon electrode.

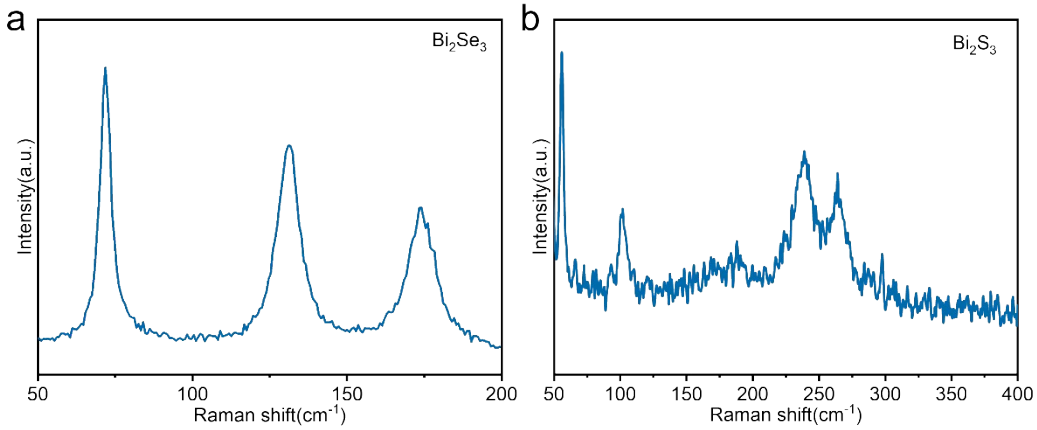

Figure S11. Raman spectra of (a) Bi_2Se_3, (b) Bi_2S_3.

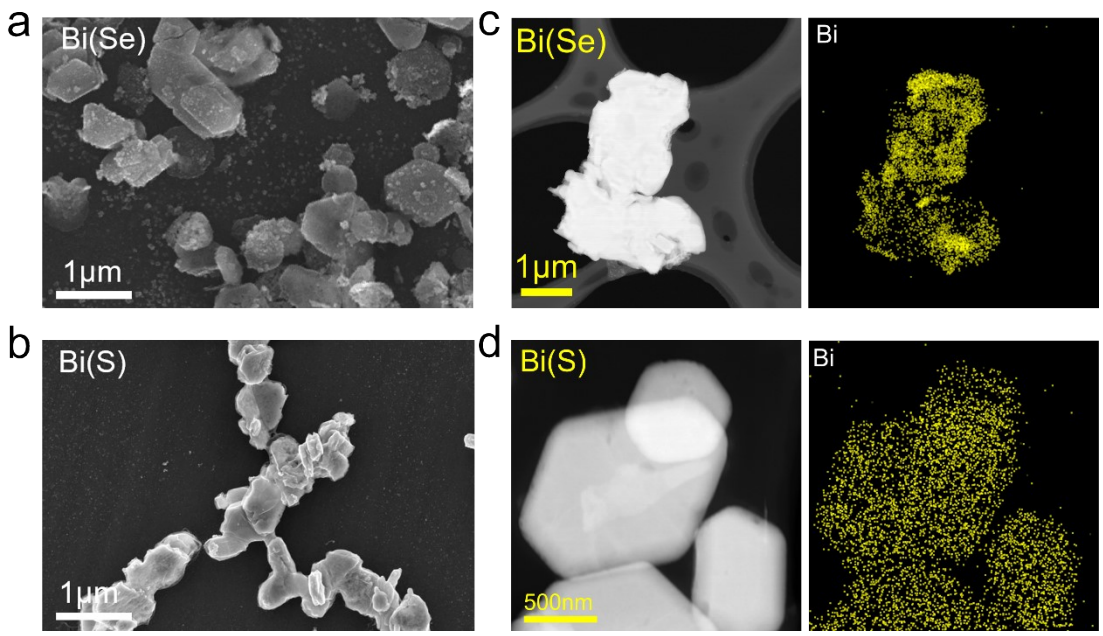

Figure S12. SEM images of (a) Bi_2Se_3, (b) Bi_2S_3. TEM images of (c) Bi(Se), (d) Bi(S), and EDS elemental maps.

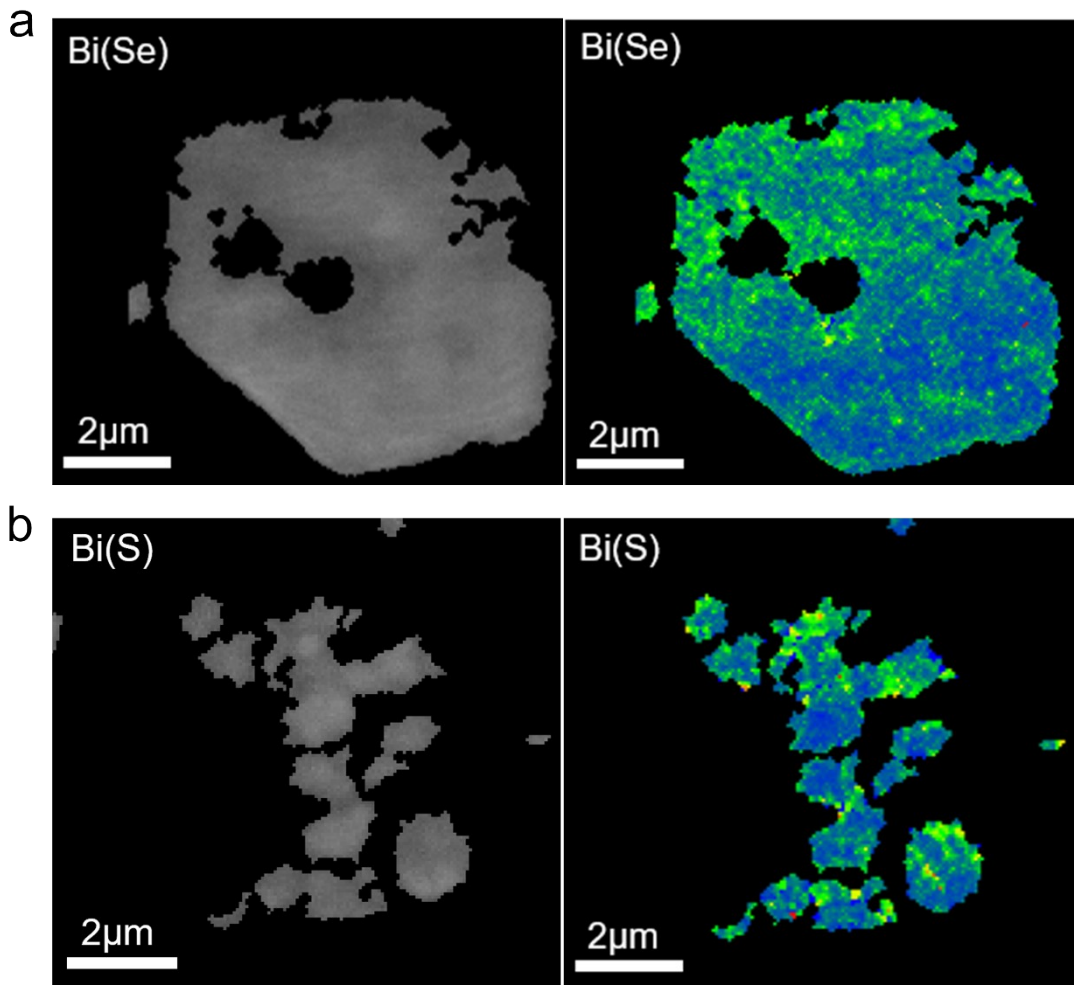

Figure S13. BC maps and KAM maps of (a) Bi(Se), (b) Bi(S).

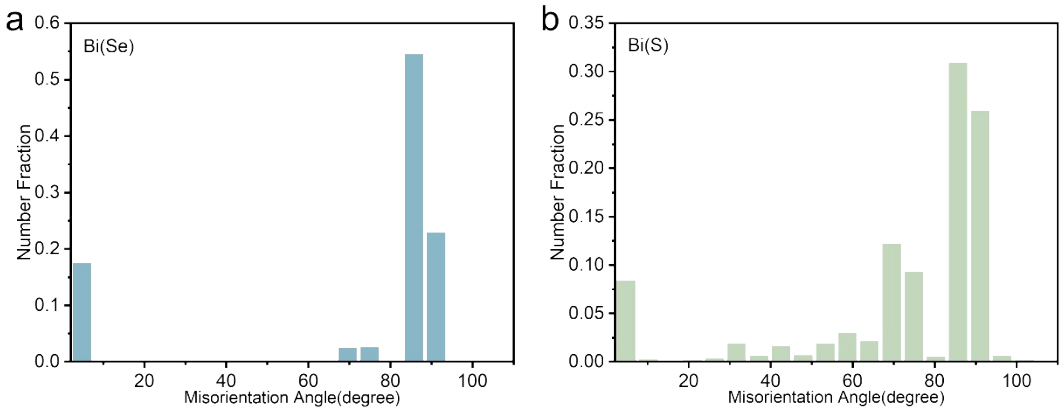

Figure S14. Proportion of the misorientation angle for (a) Bi(Se), (b) Bi(S).

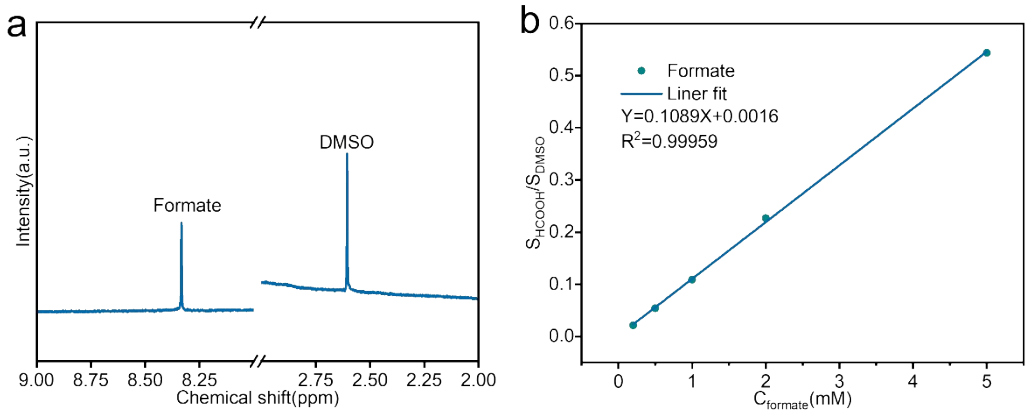

Figure S15. (a) ^{1}H NMR spectrum of formate. (b) Calibration curve for formate concentration.

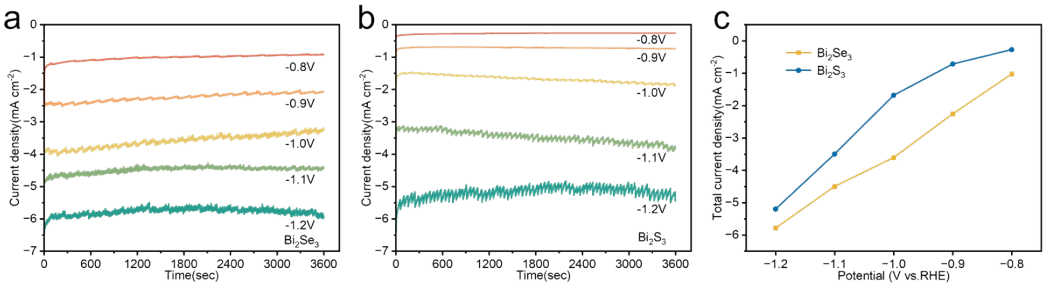

Figure S16. Total current density versus time curve at the (a) Bi(Se), (b) Bi(S) test potential. (c) Total current density at the test potential.

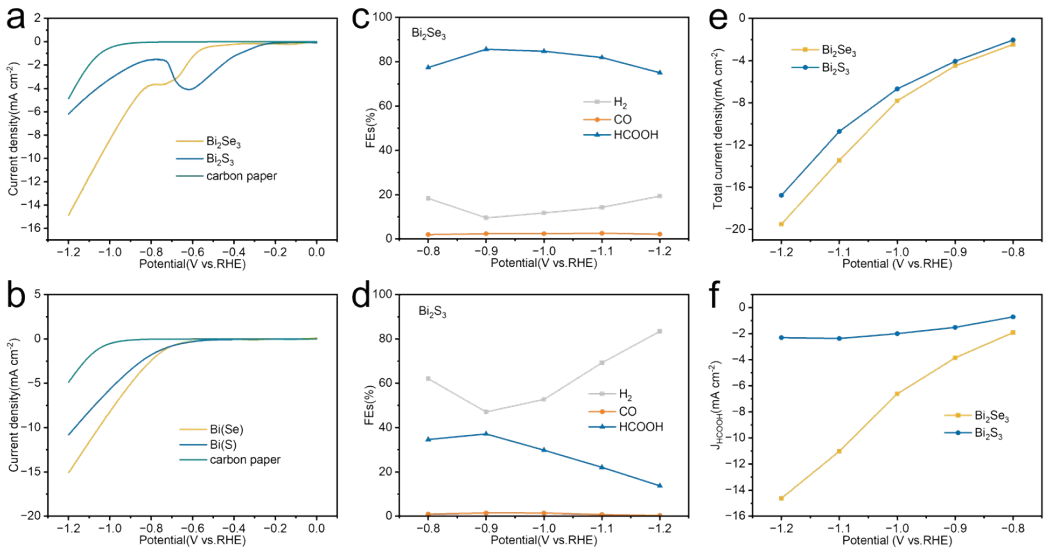

Figure 17. (a) LSV curves of Bi_2Se_3, Bi_2S_3, and carbon paper using an H-type cell at the scan rate of 10 mV s^{-1} in CO_2-saturated 0.5 M $KHCO_3$ solution. (b) LSV curves of Bi(Se), Bi(S), and carbon paper using an H-type cell at the scan rate of 10 mV s^{-1} in CO_2-saturated 0.5 M $KHCO_3$ solution. Faradaic efficiency of formate, CO, and H_2 from -0.8 to -1.2 V vs. RHE in (c) Bi(Se), (d) Bi(S) using an H-type cell. (e) Total current density at the test potential. (f) Partial current densities for formate.

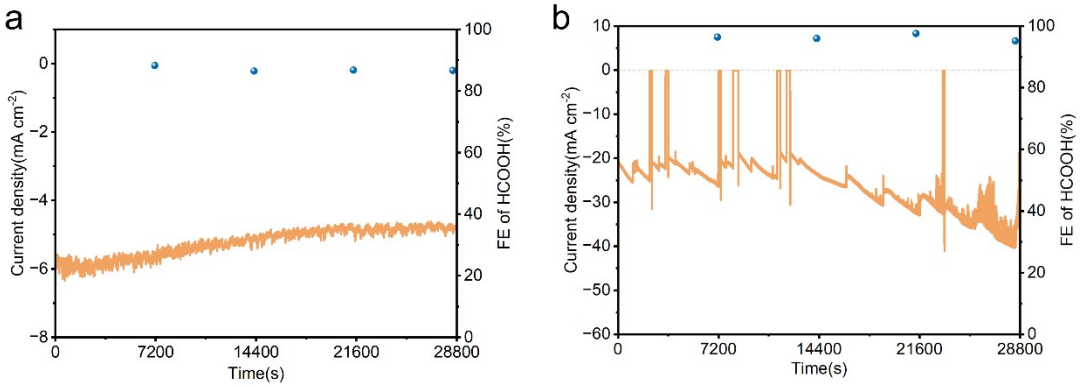

Figure S18. (a) Chronoamperometric current density and corresponding Faradaic efficiency toward formate for Bi(Se) at -1.0 V versus RHE in an H-type cell. (b) Chronoamperometric current density and corresponding Faradaic efficiency toward formate for Bi(Se) at -1.2 V versus RHE in a GDE cell.

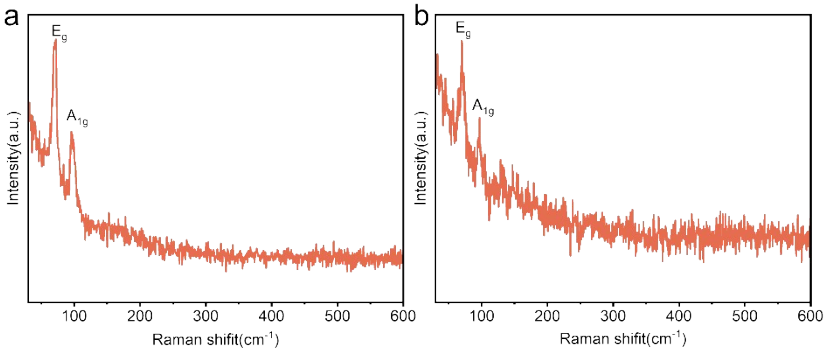

Figure S19. Raman images of Bi(Se) (a) in an H-type cell; (b)in a GDE cell.

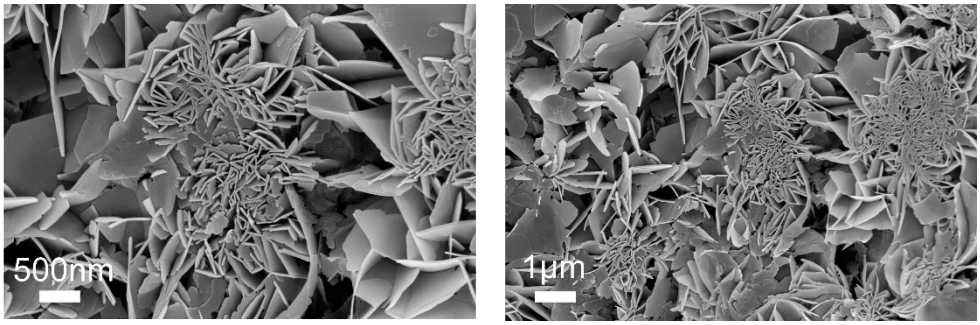

Figure S20. SEM images of Bi(Se) after prolonged testing in an H-type cell.

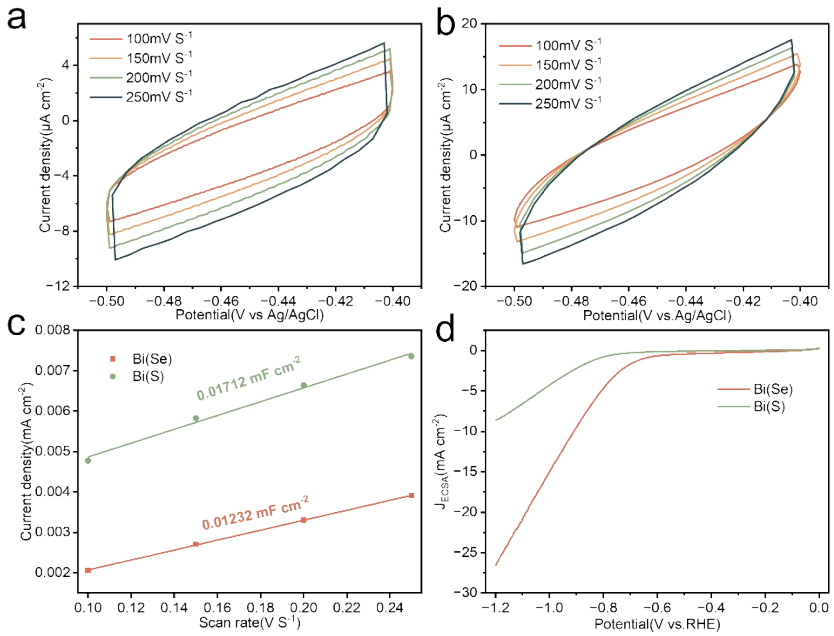

Figure S21. CV curves at varying scan rates for ECSA measurements of (a) Bi(Se), (b) Bi(S) in CO_2-saturated 0.5 M $KHCO_3$. (c) Plots of charging current density at -0.35 V vs Ag/AgCl after catalysis versus scan rate for all samples to determine the double-layer capacitance (C_{dl}). (d) The LSV curves were normalized by the ECSA to assess the intrinsic catalytic activity of the catalyst.

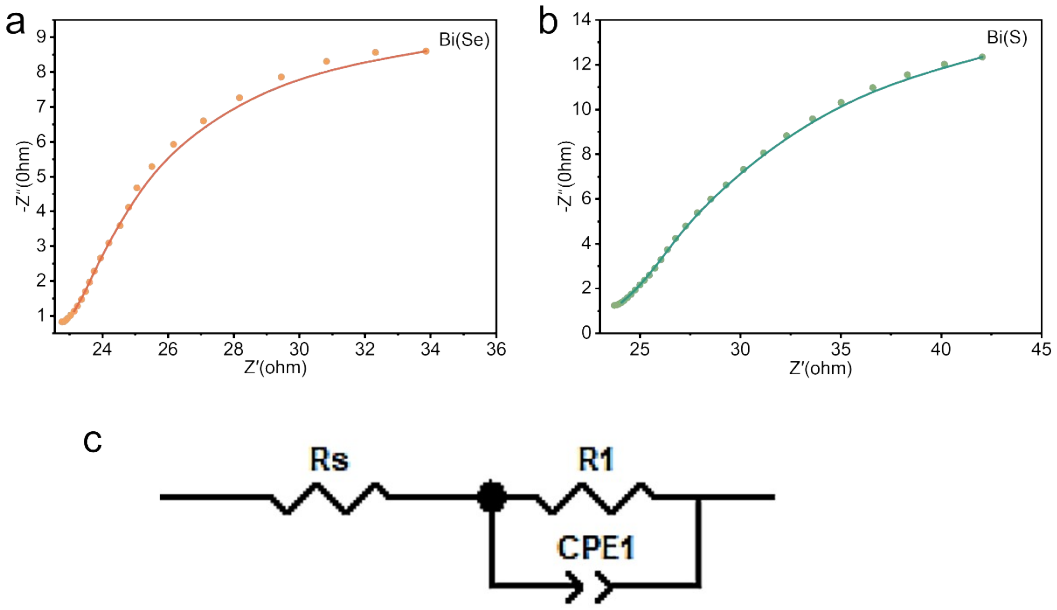

Figure S22. Nyquist plots (a) Bi(Se), (b) Bi(S) measured at -1.0 V vs RHE in CO_2-saturated 0.5 M $KHCO_3$. (c) Corresponding impedance fitting circuit diagram.

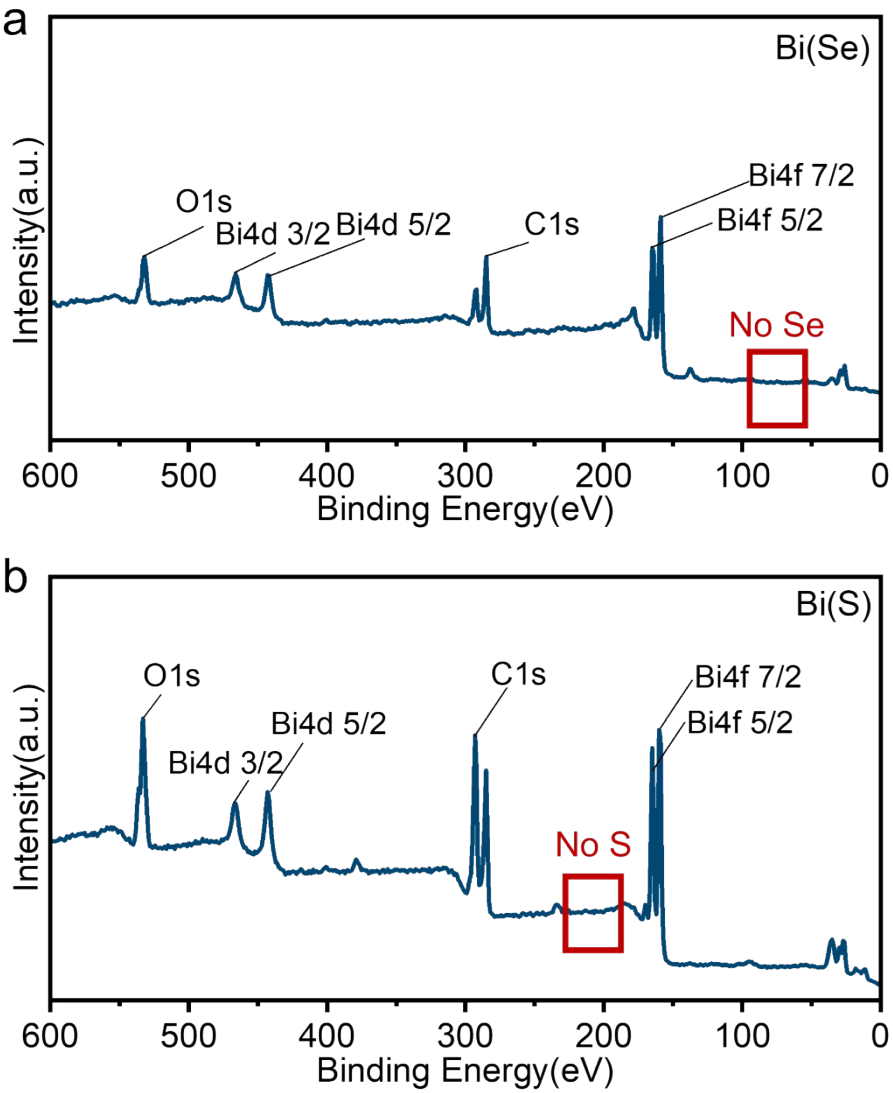

Figure S23. Full spectra of the high-resolution XPS profiles for (a) Bi(Se), (b) Bi(S).

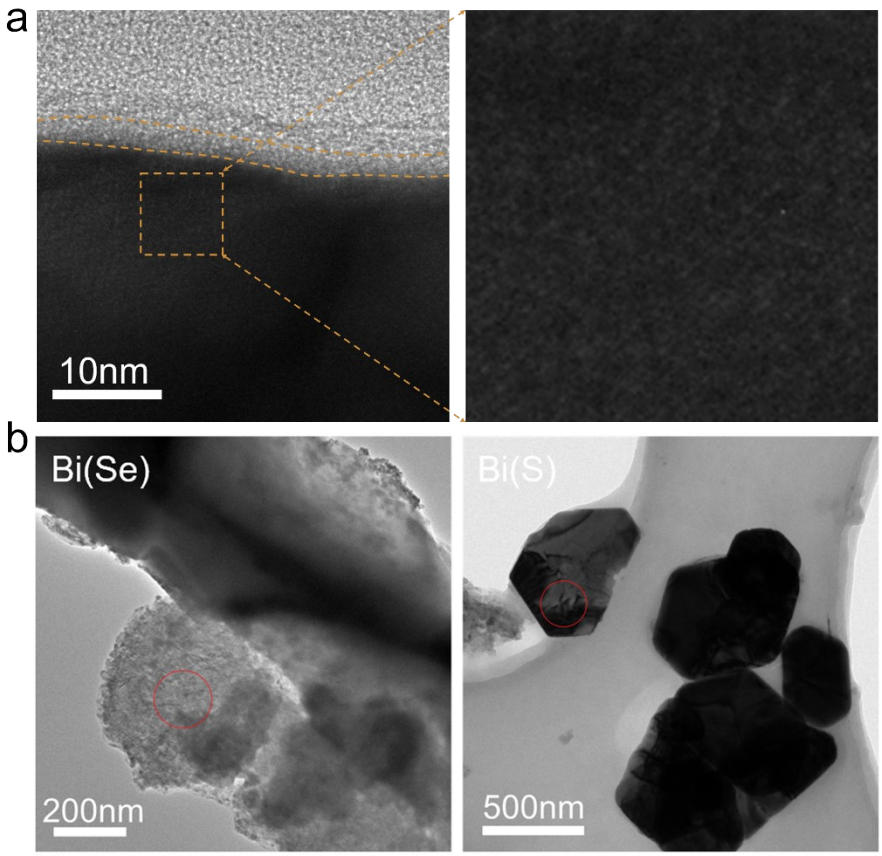

Figure S24. (a) HRTEM images of Bi(S) revealing an oxidative layer at the nanosheet edges. (b) TEM images of the SAED corresponding to Figures 2f and 2g.

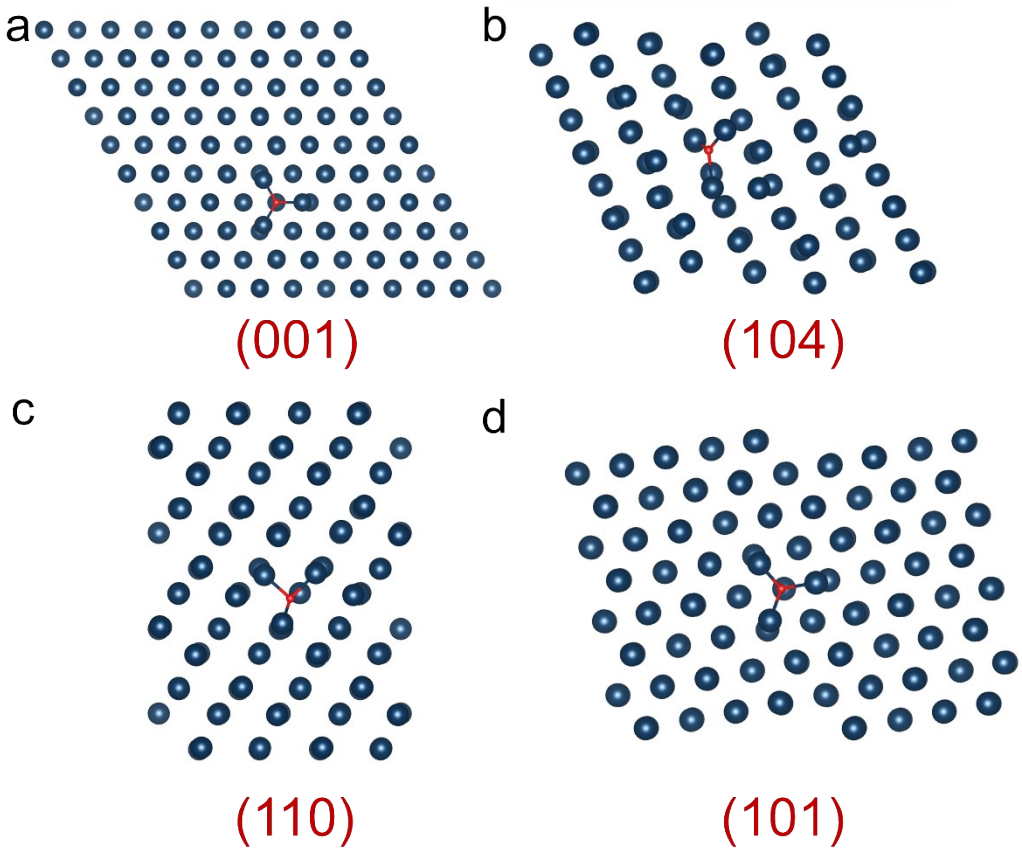

Figure S25. Models of lattice oxygen coordination on different crystal facets.

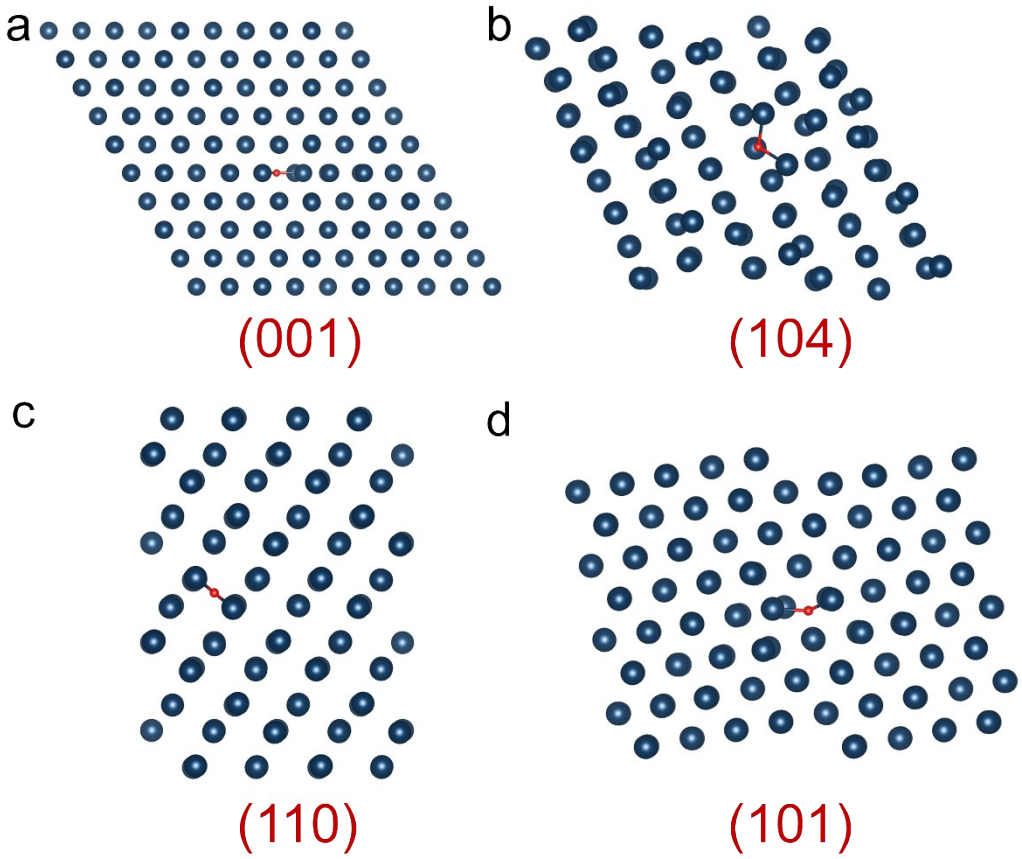

Figure S26. Models of defective oxygen coordination on different crystal facets.

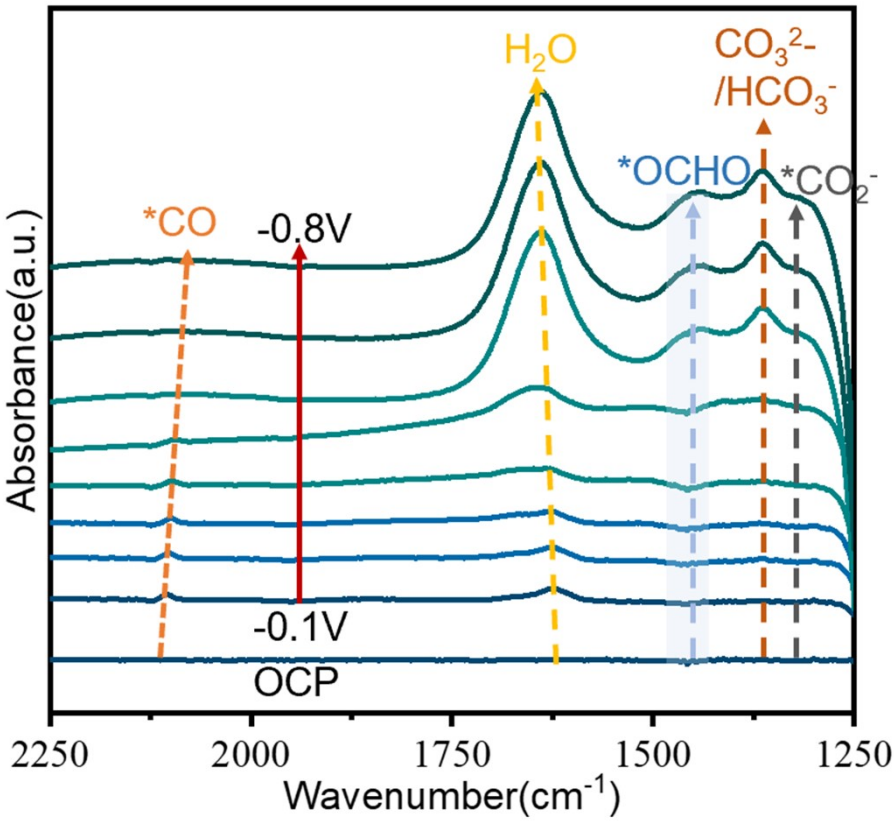

Figure S27. Operando ATR-FTIR spectra of Bi(Se) collected under applied potentials.

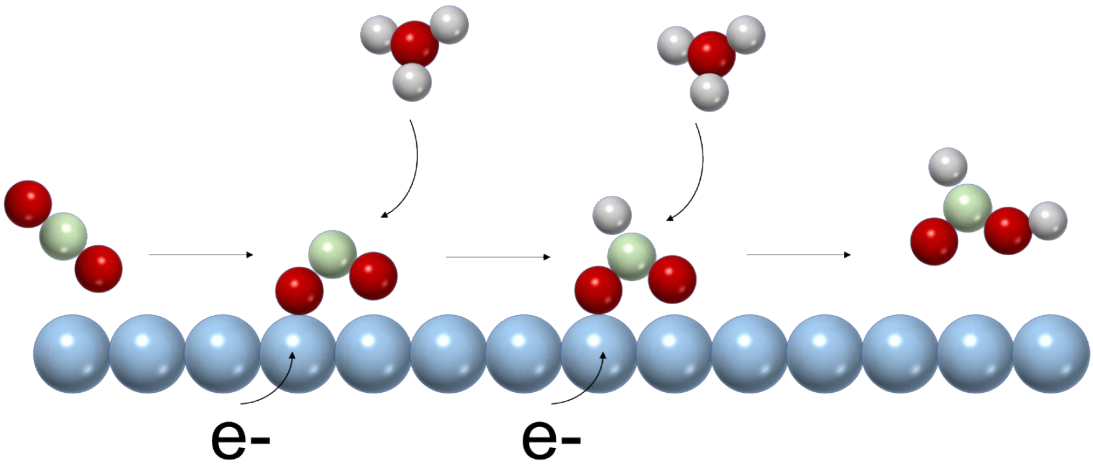

Figure S28. Schematic illustration of the carbon dioxide reduction mechanism.